Chiral magnons in altermagnetic RuO_2

Libor Šmejkal,[1,2] Alberto Marmodoro,[2] Kyo-Hoon Ahn,[2] Rafael González-Hernández,[3,1] Ilja Turek,[4] Sergiy Mankovsky,[5] Hubert Ebert,[5] Sunil W. D'Souza,[6] Ondřej Šipr,[2] Jairo Sinova,[1,2] and Tomáš Jungwirth[2,7]

[1] *Institut für Physik, Johannes Gutenberg Universität Mainz, D-55099 Mainz, Germany*
[2] *Institute of Physics, Czech Academy of Sciences, Cukrovarnická 10, 162 00 Praha 6 Czech Republic*
[3] *Grupo de Investigación en Física Aplicada, Departamento de Física,Universidad del Norte, Barranquilla, Colombia*
[4] *Institute of Physics of Materials, Czech Academy of Sciences, Zizkova 22, CZ-616 62 Brno, Czech Republic*
[5] *Department of Chemistry, Ludwig-Maximilians-University Munich, Butenandtstrasse 11, D-81377 Munich, Germany*
[6] *New Technologies-Research Center, University of West Bohemia, Plzeň 3, CZ-30100, Czech Republic*
[7] *School of Physics and Astronomy, University of Nottingham, Nottingham NG7 2RD, United Kingdom*

(Dated: September 14, 2023)

Magnons in ferromagnets have one chirality, and typically are in the GHz range and have a quadratic dispersion near the zero wavevector. In contrast, magnons in antiferromagnets are commonly considered to have bands with both chiralities that are degenerate across the entire Brillouin zone, and to be in the THz range and to have a linear dispersion near the center of the Brillouin zone. Here we theoretically demonstrate a new class of magnons on a prototypical *d*-wave altermagnet RuO_2 with the compensated antiparallel magnetic order in the ground state. Based on density-functional-theory calculations we observe that the THz-range magnon bands in RuO_2 have an alternating chirality splitting, similar to the alternating spin splitting of the electronic bands, and a linear magnon dispersion near the zero wavevector. We also show that, overall, the Landau damping of this metallic altermagnet is suppressed due to the spin-split electronic structure, as compared to an artificial antiferromagnetic phase of the same RuO_2 crystal with spin-degenerate electronic bands and chirality-degenerate magnon bands.

The study of magnetic excitations offers an important insight into fundamental properties of distinct phases of matter, as well as into applications of magnetic materials. While incoherent magnons contribute to the heat conversion and harvesting phenomena studied in the field of spin-caloritronics [1, 2], coherent magnons play a key role in the complementary field of magnonics [3–7]. This research field aims at energy-efficient transmission, storage, and processing of information without the need of charge transport, thus eliminating Joule heating and associated losses. A complete suppression of the motion of both electron and ion charges is an approach towards energy downscaling that is unparalleled in the conventional micro- and opto-electronics [5–7]. Moreover, compared to photons at the same frequency, the wavelength of magnons is orders of magnitude shorter which opens a prospect of wave-based information technology scaled down to nanometers.

Ferromagnetic magnons are polarized with a right-handed (counter-clockwise) chirality and, therefore, can carry spin currents which is the key enabling feature for magnon spintronics [4]. However, the quadratic ferromagnetic-magnon dispersion implies a wavevector-dependent group velocity. This hinders a propagation of magnon pulses in the form of stable narrow wave-packets. In addition, ferromagnetic magnonics operates primarily in the GHz range, i.e., at much slower rates than those offered by photonics.

In contrast, as schematically illustrated in Fig. 1, antiferromagnetic magnons typically have a photon-like linear dispersion close to the center of the magnonic Brillouin zone when neglecting relativistic effects, and reach the THz frequencies [8, 9]. However, in the conventional collinear antiferromagnets with two mutually compensating opposite-spin sublattices, the corresponding two polarized magnon modes with right-handed and left-handed chirality are degenerate across the entire Brillouin zone [10–13]. The observation of magnon-generated spin currents in antiferromagnets then relied on the splitting of the degeneracy of the opposite-chirality modes by externally applied magnetic fields [11, 12].

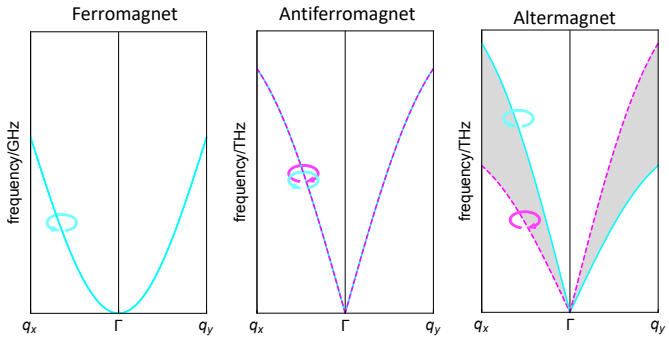

FIG. 1. Schematic representation of the distinct phenomenologies of non-relativistic magnon spectra in three basic classes of collinear magnets. Left: A polarized magnon mode with a right-handed (counter-clockwise, cyan) chirality and a quadratic dispersion near the **Γ**-point in a ferromagnet. Middle: Two degenerate magnon modes with right-handed and left-handed (clockwise, purple) chirality and linear dispersion near the **Γ**-point in an antiferromagnet. Right: Alternating splitting (highlighted by grey shading) of two magnon modes with right-handed and left-handed chirality and linear dispersion near the **Γ**-point in an altermagnet.

In our Letter we demonstrate distinct characteristics of magnons in altermagnets [15, 16] that can remove the above principal limitations of ferromagnets and antiferromagnets. Confirmed by density-functional-theory (DFT) calculations, we show that in this recently identified third basic magnetic class [15, 16], the magnon modes with right-handed and left-handed chirality can be split at zero magnetic field despite the vanishing net equilibrium magnetization of these unconventional collinear compensated magnets. The sign of the splitting between the opposite-chirality modes alternates across the magnon Brillouin zone (see schematic illustration in Fig. 1), similar to the alternating sign of the spin splitting of the electronic bands [15, 16].

We predict that the magnitude of the splitting between the opposite-chirality modes in altermagnetic RuO_2 reaches a $\sim$ 10 meV range. This scale is comparable to the splitting between opposite-chirality modes in an uncompensated ferrimagnet YIG [17]. We also point out that a direct experimental detection of the mode chirality for splittings on the $\sim 1-10$ meV scale has become recently accessible via inelastic polarized neutron scattering [17].

While altermagnets can have the ferromagnetic-like (ferrimagnetic-like) separate polarized magnon modes with a certain chirality they, simultaneously, preserve the favorable antiferromagnetic-like THz-range and linear dispersion of the magnon modes (see schematic illustration in Fig. 1). The alternating sign of the chirality splitting is a unique signature of altermagnetic magnons with no counterpart in conventional ferromagnets or antiferromagnets.

We start our discussion with symmetry-based remarks. The typically leading contribution to the magnon spectra can be obtained by mapping the spin-dependent electronic structure on the non-relativistic Heisenberg Hamiltonian, $H = -\sum_{i \neq j} J_{ij} \hat{\mathbf{e}}_i \cdot \hat{\mathbf{e}}_j$ [13, 18–21]. Here $\hat{\mathbf{e}}_i$ is the direction of the magnetic moment for an atom at position $\mathbf{R}_i$, and J_{ij} are Heisenberg exchange coupling parameters. In the Heisenberg model, the real and spin space transformations are decoupled and the symmetries of the corresponding magnon bands can be described by the non-relativistic spin-group formalism [10, 13, 14].

In antiferromagnets, crystallographic translation or inversion symmetry transformations connecting opposite-spin sublattices protect the degeneracy of the magnon bands with the opposite chirality [10, 13]. Remarkably, this has been commonly illustrated on the opposite-spin sublattices of rutile crystals, while omitting the presence of non-magnetic atoms in these crystals [9, 10, 13]. However, as highlighted in recent theoretical studies of the electronic structure of the metallic rutile RuO_2, the non-magnetic O-atoms break the translation and inversion symmetries connecting the opposite-spin sublattices [15, 16, 22]. The remaining symmetries connecting the opposite-spin sublattices, that protect the zero net magnetization in the non-relativistic limit, are crystallographic (proper or improper) rotations [15, 16]. The symmetries of RuO_2 allow for the relativistic anomalous Hall effect [22, 23], and for non-relativistic spin currents [24–27], giant and tunneling magnetoresitance [28, 29], and spin-split band structure [15, 30]. Instead of classical antiferromagnetism [9, 10, 13, 31], the rutiles, including RuO_2, are the prototypical representatives of altermagnetism according to the recent spin-group symmetry classification of collinear magnetic phases [15].

We now proceed to the *ab initio* calculations of the magnon spectra in RuO_2. First we map the DFT electronic band structure on the Heisenberg Hamiltonian and obtain the chirality-split, as well as the chirality-degenerate, parts of the spectrum of the undamped magnons across the RuO_2 Brillouin zone. Next, we include into the consideration also the spectrum of Stoner excitations, which is expected to provide the leading mechanism limiting the lifetime of magnons [21, 32] in metallic RuO_2. On one hand, the spin-split parts of the electronic band structure are expected to suppress this Landau damping, in analogy to ferromagnets [21, 32–34]. On the other hand, the altermagnetic spin-group symmetries also protect the presence of spin-degenerate nodal surfaces crossing the $\mathbf{\Gamma}$-point [15, 16], and these can be expected to generate an antiferromagnetic-like enhancement of the Landau damping. We will qualitatively estimate the strength of the Landau damping in the altermagnetic phase of RuO_2 by comparing it to the calculated magnon lifetime in an artificial antiferromagnetic phase of the same RuO_2 crystal with spin-degenerate electronic bands and chirality-degenerate magnonic bands across the entire Brillouin zone.

In the DFT electronic-structure calculations [35], we consider the experimental lattice parameters of RuO_2, taken from Ref. [36] (for more details see Supplementary information). The magnon spectra of RuO_2 were produced by mapping the DFT results onto the Heisenberg Hamiltonian and by diagonalizing the associated Landau-Lifschitz equation of motion for the adiabatic magnon dispersion. The coupling parameters were determined using the magnetic force theorem [18], as detailed in Ref. [20]. For the DFT-based calculation of the Landau damping we adopt the approximation of Ref. [21]. (For more details see Supplementary information.)

In Fig. 2a we show the rutile crystal structure of RuO_2 (see also Supplementary information further highlighting the positions and spacings of Ru atoms in the crystal). The calculated pairwise Heisenberg exchange interaction parameters among different sets of Ru atoms mutually separated by $|\mathbf{R}_{ij}|$ are shown in Fig 2b. Among those, we observe that all inter-sublattice exchange interactions are negative or negligibly small. The resulting compensated antiparallel ordering is consistent with experimental neutron scattering data on RuO_2 [37]. The equal value of

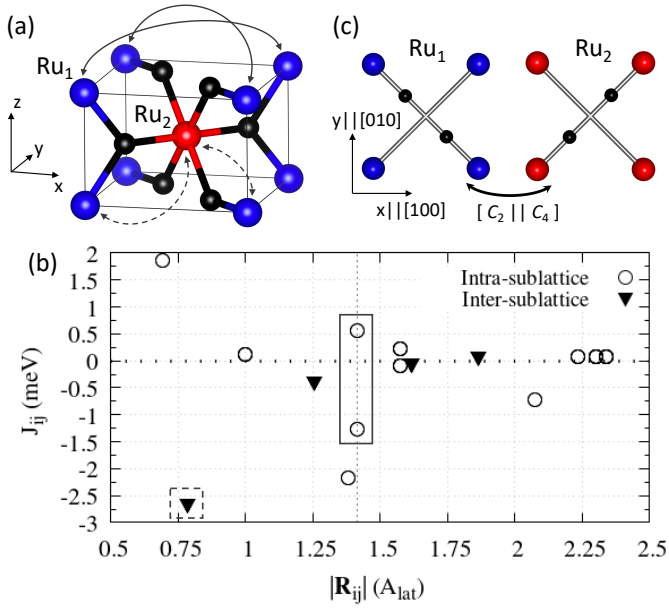

FIG. 2. (a) Model of the crystal structure of the altermagnetic rutile phase of RuO_2. The opposite-spin sublattices are labeled by Ru_1 and Ru_2 and further distinguished by the blue and red color. The black spheres correspond to O atoms. Inter/intra-sublattice exchange interactions between pairs of Ru atoms, discussed in the text, are highlighted by dashed/solid double-arrow curves. (b) DFT Heisenberg exchange parameters as a function of the separation of Ru atoms. The dashed/solid rectangle highlights the exchange parameters corresponding to the dashed/solid double-arrow curves in panel (a). (Only exchange parameters with energy cut-off above 3 meV are shown.) (c) The opposite spin sublattices with the highlighted spin-group symmetry of the altermagnetic RuO_2, which combines a two-fold spin-space rotation C_2 with a four-fold crystallographic-space rotation C_4 (four-fold screw-axis parallel to the c-axis).

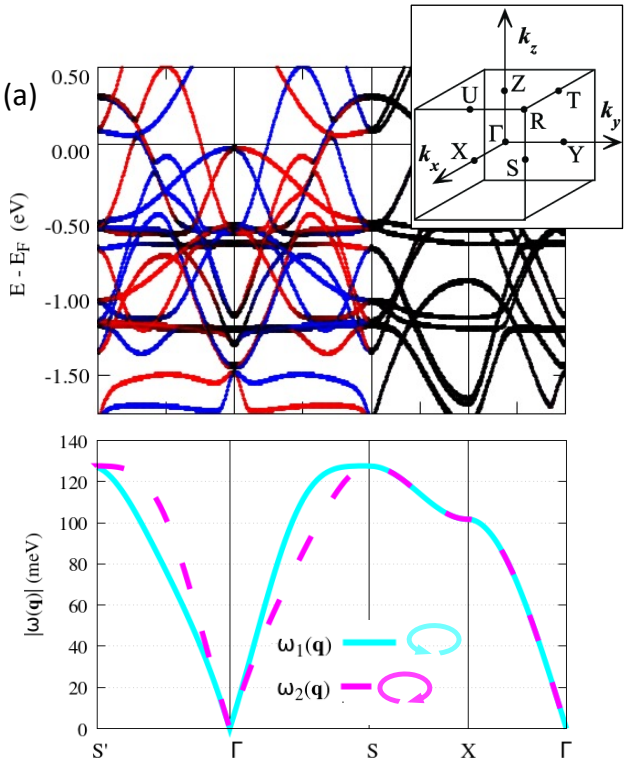

FIG. 3. Top: Electronic band structure of the altermagnetic phase of RuO_2 plotted along a Brillouin zone path in a $k_x - k_y$ plane crossing the $\mathbf{\Gamma}$-point. Red and blue colors mark projections on opposite-spin channels. Bottom: Corresponding magnonic band structure. Purple and cyan colors mark opposite magnon chiralities. (

the two nearest-neighbor inter-sublattice exchange parameters, represented in Fig. 2b by a single triangle highlighted by a dashed rectangle and corresponding to the two dashed double-arrows in Fig. 2a, illustrates the C_4 symmetry connecting the opposite-spin sublattices in the RuO_2 crystal (Fig 2c) that is preserved in the microscopic DFT Hamiltonian and in the Heisenberg model. Here C_4 represents a four-fold screw-axis parallel to the crystallographic c-axis.

Next we analyze the intra-sublattice exchange parameters. Among those, the ones corresponding to Ru atoms separated by $\sqrt{2}\ A_{lat}$ play a decisive role in the resulting alternating chirality-splitting of the magnon spectra, plotted in Fig. 3 side-by-side the spin-split electronic bands. (A_{lat} denotes the $x-y$ plane lattice constant, see Supplementary information.) These J_{ij}'s are highlighted in Fig. 2b by a solid rectangle and correspond to the pairs of Ru atoms connected by solid double-arrow curves in Fig 2a. They are sizable in magnitude when compared to the first and second-nearest-neighbour exchange parameters (owing to the itinerant origin of magnetism in RuO_2) shown in Fig. 2b. However, unlike the latter, the intra-sublattice J_{ij}'s for Ru atoms separated by $|\mathbf{R}_{ij}| = \sqrt{2}\ A_{lat}$ depend on the direction of $\mathbf{R}_{ij}$. They have a different magnitude and even opposite sign, depending on whether the exchange interaction acts along the $y = -x$ or along the 90°-rotated $y = +x$ diagonal. We attribute the strong dependence of these J_{ij} parameters on the direction of $\mathbf{R}_{ij}$ to the presence or absence of the O atoms along the corresponding bonds, as seen in Fig. 2a.

The electronic and magnonic band dispersions along Brillouin zone lines in the $k_x - k_y$ planes crossing the $\mathbf{\Gamma}$-point are shown in Fig. 3, and the $\mathbf{Z}$-point in Supplementary information. There are two magnon eigenmodes, $\omega_n(\mathbf{q})$, reflecting the number of magnetic sublattices. The corresponding eigenfrequency of the wave-like angular precession has opposite sign along the two branches, i.e., it describes clockwise or anti-clockwise rotation of the Ru atomic moments around the $\hat{z}$-axis (the easy c-axis of the magnetic moments in RuO_2 [22, 23, 37]). In either case, the excitation of magnons requires to supply energy into the system, proportional to $|\omega_n(\mathbf{q})|$.

In the Supplementary information, we highlight the magnitude of the corresponding magnon eigenvector

components, which indicates how much each of the two opposite-spin Ru sublattices have their moments tilted away from the $\hat{z}$-direction, i.e., from the ground state order [19]. This representation shows how the excitations involve the opposite-spin sublattices in different fashion as a function of the wavevector $\mathbf{q}$ within the Brillouin zone. Near the $\mathbf{\Gamma}$-point, the collective precession affects to the same extent the magnetic moments of both Ru sublattices. In contrast, towards the boundary of the Brillouin zone, each eigenmode is dominantly carried by one or the other Ru sublattice, respectively.

The key observation in Fig. 3 is that the opposite-chirality magnonic bands can be split, as illustrated by calculations along the $\mathbf{\Gamma}-\mathbf{S}$ path (for the $\mathbf{Z}-\mathbf{R}$ path see Supplementary information). The chirality splitting of the magnonic bands is similar to the spin-splitting of the electronic bands along the same paths. Magnon excitations of one chirality eigenmode occur at a larger energy cost than for the opposite chirality. The order gets reversed along the orthogonal directions $\mathbf{\Gamma}-\mathbf{S}'$ (Fig. 3) and $\mathbf{Z}-\mathbf{R}'$ (Supplementary information). This is again similar to the alternating sign of the spin splitting observed in the electronic band structure. The alternating sign of the chirality splitting and spin splitting imposes that the magnonic and electronic bands are spin degenerate in parts of the Brillouin zone. In Fig. 3, this is illustrated along the $\mathbf{S}-\mathbf{X}-\mathbf{\Gamma}$ path (and in the Supplementary information along the $\mathbf{R}-\mathbf{U}-\mathbf{Z}$ path).

We can numerically track the origin of the chirality splitting to the directionality dependence in the Heisenberg exchange interaction discussed above, accounting for the contribution of the exchange couplings within spheres of different radii. For $|\mathbf{R}_{ij}|< \sqrt{2}A_{lat}$, the J_{ij} parameters depend only on the distance (see Fig. 2b). Calculations of the magnon dispersion truncating the lattice Fourier transformation to this shorter cutoff produce no lifting of the degeneracy of the opposite-chirality magnon bands. On the other hand, the anisotropy of some of the exchange interactions (e.g. those highlighted in Fig. 2a by solid double-arrow curves) generates the chirality splitting of the magnon eigenmodes in the RuO_2 altermagnet.

We emphasize that the anisotropy of the exchange interactions alone is not sufficient for generating a chirality-split magnon spectrum. The anisotropy has to be accompanied by the spin-group symmetries of the altermagnetic phase of RuO_2. To highlight this point, we have performed reference calculations for an artificial antiferromagnetic phase of RuO_2, constructed from the altermagnetic phase by doubling the unit cell along the z-axis, which introduces an additional translation symmetry connecting the opposite-spin sublattices (see Supplementary information). Despite the persisting anisotropy of some of the J_{ij}'s, the spin-group symmetry of this antiferromagnetic phase protects the spin-degeneracy of the electronic bands across the whole Brillouin zone [15, 16]. Our DFT calculations shown in the Supplementary information confirm the corresponding chirality-degeneracy of the magnon bands.

Another important observation in Fig. 3 is the linear energy dependence $|\omega_n(\mathbf{q})|\propto|\mathbf{q}|$ over a significant portion of the Brillouin zone, and the THz range of the altermagnetic magnons in RuO_2. This is analogous to the conventional magnon dispersions in antiferromagnets [8, 9], and contrasts with the quadratic dispersion and GHz range typical of ferromagnetic magnons.

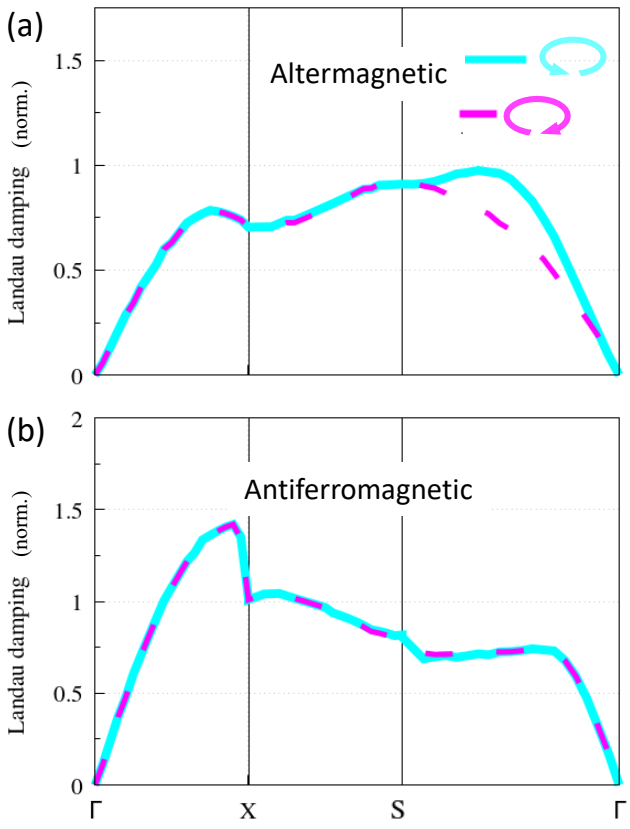

FIG. 4. Comparison of the Landau damping in the altermagnetic (a) and artificial antiferromagnetic (b) phase of RuO_2, normalized to the maximum Landau damping in the altermagnetic phase for the depicted path in the Brillouin zone. Purple and cyan colors mark opposite magnon chiralities

We conclude the discussion of the chirality splitting of magnon modes in altermagnets by noting that we observe a negligible effect on the splitting when mapping the DFT electronic structure on a generalized Heisenberg model that includes relativistic spin-orbit coupling effects [38]. For more details see Supplementary information. We also show in the Supplementary information our calculations of the alternating chirality splitting of magnon modes in an insulating rutile CoF_2, in hematite Fe_2O_3, and in semiconducting MnTe, that all have been classified by symmetry as altermagnets [15, 16]. The calculations confirm that the alternating chirality splitting

is a general feature of magnon spectra in altermagnets, and highlight that the magnitude of the splitting can be strongly material dependent (for more details see Supplementary information).

We now move on to the discussion of the Landau damping in RuO_2, determined by the intensity of Stoner single-particle spin-flip transitions. The approximated Landau damping calculated by the method described in Ref. [21] and in the Supplementary information is shown in Fig. 4. The intensity of Stoner single-particle spin-flip transitions is degenerate along the $\mathbf{S} - \mathbf{X} - \mathbf{\Gamma}$ path, or non-degenerate along the $\mathbf{\Gamma} - \mathbf{S}$ path, in the same way as observed for the magnon dispersion $\omega_n(\mathbf{q})$ in Figs. 3. In Figs. 4 we qualitatively compare the Landau damping calculated along the above Brillouin zone paths for the altermagnetic phase of RuO_2 and for the artificial antiferromagnetic phase. In both panels, the data are normalized to the maximum value of the Landau damping in the altermagnetic phase for the depicted path in the Brillouin zone. As expected, the antiferromagnetic phase leads to the degeneracy in the Landau damping of the opposite-chirality magnon eigenmodes. As also anticipated from the spin degenerate band structure over the entire Brillouin zone, the Landau damping tends to be, overall, stronger in the antiferromagnetic phase.

Near the $\mathbf{\Gamma}$ point, the calculated Landau damping in the altermagnetic phase of RuO_2 shows a non-zero intensity of the competing Stoner excitations, which is analogous to the behavior of metallic antiferromnagnets [33]. In comparison, metallic ferromagnets present a Stoner gap, i.e., no Landau damping for $\mathbf{q} \to \mathbf{\Gamma}$. This is a consequence of the splitting of the electronic bands into majority and minority-spin states. Single-particle spin-flip transitions that can compete with the collective magnetic excitations are only possible upon overcoming the above gap [33]. In the altermagnetic phase of RuO_2, the electronic bands over most the Brillouin-zone volume are also spin split. This explains the observed overall suppression of the Landau damping, as compared to the artificial antiferromagnetic phase. The Landau damping in altermagnetic RuO_2, therefore, shows features that are intermediate between the antiferromagnetic and ferromagnetic cases.

To conclude, we have demonstrated that similarly to the electronic band structure, the degeneracy of magnon bands with opposite chirality is lifted in altermagnetic RuO_2, with the sign of the chirality-splitting alternating across the magnon Brillouin zone. This indicates that, on one hand, magnons in altermagnets can be chiral and carry spin currents, similar to ferromagnets but with highly anisotropic characteristics. On the other hand, the dispersion of altermagnetic magnons can be linear over a significant portion of the Brillouin zone, similar to antiferromagnets. These unconventional characteristics make altermagnets a promising material platform for spin-caloritronics [39] and magnonics. The latter research direction may include the exploration of the emission, propagation and detection of ultra-short (ps-scale) pulses of chiral THz magnons of wavelengths orders of magnitude smaller than the wavelengths of the THz photons.

ACKNOWLEDGMENTS

We acknowledge funding from the Czech Science Foundation Grant No. 19-18623X and 19-06433S, the Ministry of Education of the Czech Republic Grants No. LM2018096, LM2018110, LM2018140, and LNSM-LNSpin, and the EU FET Open RIA Grant No. 766566, Deutsche Forschungsgemeinschaft Grant TRR 173 268565370 (project A03), the computing time supported by the project CEDAMNF CZ.02.1.01/0.0/0.0/15_003/0000358 (Ministry of Education,Youth and Sport) and by the "Information Technology for Innovation" (IT4I) grant OPEN-22-42, and granted on the supercomputer Mogon at Johannes Gutenberg University Mainz (hpc.uni-mainz.de) and the support of Alexander Von Humboldt Foundation.

[1] G. E. W. Bauer, E. Saitoh, and B. J. van Wees, Nature Materials **11**, 391 (2012).
[2] M. Mizuguchi and S. Nakatsuji, Science and Technology of Advanced Materials **20**, 262 (2019).
[3] S. Neusser and D. Grundler, Advanced Materials **21**, 2927 (2009).
[4] A. V. Chumak, V. I. Vasyuchka, A. A. Serga, and B. Hillebrands, Nature Physics **11**, 453 (2015).
[5] D. Sander, S. O. Valenzuela, D. Makarov, C. H. Marrows, E. E. Fullerton, P. Fischer, J. McCord, P. Vavassori, S. Mangin, P. Pirro, B. Hillebrands, A. D. Kent, T. Jungwirth, O. Gutfleisch, C. G. Kim, and A. Berger, Journal of Physics D: Applied Physics **50**, 363001 (2017).
[6] P. Pirro, V. I. Vasyuchka, A. A. Serga, and B. Hillebrands, Nature Reviews Materials **6**, 1114 (2021).
[7] A. V. Chumak, P. Kabos, M. Wu, C. Abert, C. Adelmann, A. O. Adeyeye, J. Akerman, F. G. Aliev, A. Anane, A. Awad, C. H. Back, A. Barman, G. E. Bauer, M. Becherer, E. N. Beginin, V. A. Bittencourt, Y. M. Blanter, P. Bortolotti, I. Boventer, D. A. Bozhko, S. A. Bunyaev, J. J. Carmiggelt, R. R. Cheenikundil, F. Ciubotaru, S. Cotofana, G. Csaba, O. V. Dobrovolskiy, C. Dubs, M. Elyasi, K. G. Fripp, H. Fulara, I. A. Golovchanskiy, C. Gonzalez-Ballestero, P. Graczyk, D. Grundler, P. Gruszecki, G. Gubbiotti, K. Guslienko, A. Haldar, S. Hamdioui, R. Hertel, B. Hillebrands, T. Hioki, A. Houshang, C. M. Hu, H. Huebl, M. Huth, E. Iacocca, M. B. Jungfleisch, G. N. Kakazei, A. Khitun, R. Khymyn, T. Kikkawa, M. Klaui, O. Klein, J. W. Klos, S. Knauer, S. Koraltan, M. Kostylev, M. Krawczyk, I. N. Krivorotov, V. V. Kruglyak, D. Lachance-Quirion, S. Ladak, R. Lebrun, Y. Li, M. Lindner, R. MacEdo, S. Mayr, G. A. Melkov, S. Mieszczak, Y. Nakamura,

H. T. Nembach, A. A. Nikitin, S. A. Nikitov, V. Novosad, J. A. Otalora, Y. Otani, A. Papp, B. Pigeau, P. Pirro, W. Porod, F. Porrati, H. Qin, B. Rana, T. Reimann, F. Riente, O. Romero-Isart, A. Ross, A. V. Sadovnikov, A. R. Safin, E. Saitoh, G. Schmidt, H. Schultheiss, K. Schultheiss, A. A. Serga, S. Sharma, J. M. Shaw, D. Suess, O. Surzhenko, K. Szulc, T. Taniguchi, M. Urbanek, K. Usami, A. B. Ustinov, T. Van Der Sar, S. Van Dijken, V. I. Vasyuchka, R. Verba, S. V. Kusminskiy, Q. Wang, M. Weides, M. Weiler, S. Wintz, S. P. Wolski, and X. Zhang, IEEE Transactions on Magnetics **58** (2022), 10.1109/TMAG.2022.3149664.

[8] O. Gomonay, V. Baltz, A. Brataas, and Y. Tserkovnyak, Nature Physics **14**, 213 (2018).

[9] S. M. Rezende, A. Azevedo, and R. L. Rodríguez-Suárez, Journal of Applied Physics **126**, 151101 (2019).

[10] W. F. Brinkman and R. J. Elliott, Proceedings of the Royal Society A: Mathematical, Physical and Engineering Sciences **294**, 343 (1966).

[11] R. Cheng and Q. Niu, Physical Review B **89**, 081105 (2014), arXiv:1304.1284.

[12] J. Li, C. B. Wilson, R. Cheng, M. Lohmann, M. Kavand, W. Yuan, M. Aldosary, N. Agladze, P. Wei, M. S. Sherwin, and J. Shi, Nature **578**, 70 (2020).

[13] A. Corticelli, R. Moessner, and P. A. McClarty, Physical Review B **105**, 064430 (2022), arXiv:2103.05656.

[14] X. Chen, J. Ren, J. Li, Y. Liu, and Q. Liu, (2023), arXiv:2307.12366.

[15] L. Šmejkal, J. Sinova, and T. Jungwirth, Physical Review X **12**, 031042 (2022).

[16] L. Šmejkal, J. Sinova, and T. Jungwirth, Physical Review X **12**, 040501 (2022), arXiv:2204.10844.

[17] Y. Nambu, J. Barker, Y. Okino, T. Kikkawa, Y. Shiomi, M. Enderle, T. Weber, B. Winn, M. Graves-Brook, J. M. Tranquada, T. Ziman, M. Fujita, G. E. W. Bauer, E. Saitoh, and K. Kakurai, Physical Review Letters **125**, 027201 (2020).

[18] A. I. Liechtenstein, M. I. Katsnelson, V. P. Antropov, and V. A. Gubanov, Journal of Magnetism and Magnetic Materials **67**, 65 (1987).

[19] S. V. Halilov, H. Eschrig, A. Y. Perlov, and P. M. Oppeneer, Physical Review B **58**, 293 (1998).

[20] S. Mankovsky and H. Ebert, Physical Review B **96**, 104416 (2017), arXiv:1706.04165.

[21] A. Marmodoro, S. Mankovsky, H. Ebert, J. Minár, and O. Šipr, Physical Review B **105**, 174411 (2022).

[22] L. Šmejkal, R. González-Hernández, T. Jungwirth, and J. Sinova, Science Advances **6**, eaaz8809 (2020), arXiv:1901.00445.

[23] Z. Feng, X. Zhou, L. Šmejkal, L. Wu, Z. Zhu, H. Guo, R. González-Hernández, X. Wang, H. Yan, P. Qin, X. Zhang, H. Wu, H. Chen, Z. Meng, L. Liu, Z. Xia, J. Sinova, T. Jungwirth, and Z. Liu, Nature Electronics **5**, 735 (2022), arXiv:2002.08712.

[24] R. González-Hernández, L. Šmejkal, K. Výborný, Y. Yahagi, J. Sinova, T. Jungwirth, and J. Železný, Physical Review Letters **126**, 127701 (2021), arXiv:2002.07073.

[25] A. Bose, N. J. Schreiber, R. Jain, D.-f. Shao, H. P. Nair, J. Sun, X. S. Zhang, D. A. Muller, E. Y. Tsymbal, D. G. Schlom, and D. C. Ralph, Nature Electronics **5**, 263 (2022), arXiv:2108.09150.

[26] H. Bai, L. Han, X. Y. Feng, Y. J. Zhou, R. X. Su, Q. Wang, L. Y. Liao, W. X. Zhu, X. Z. Chen, F. Pan, X. L. Fan, and C. Song, Physical Review Letters **128**, 197202 (2022), arXiv:2109.05933.

[27] S. Karube, T. Tanaka, D. Sugawara, N. Kadoguchi, M. Kohda, and J. Nitta, Physical Review Letters **129**, 137201 (2022), arXiv:2111.07487.

[28] L. Šmejkal, A. B. Hellenes, R. González-Hernández, J. Sinova, and T. Jungwirth, Physical Review X **12**, 011028 (2022), arXiv:2103.12664.

[29] D.-F. Shao, S.-H. Zhang, M. Li, C.-B. Eom, and E. Y. Tsymbal, Nature Communications **12**, 7061 (2021), arXiv:2103.09219.

[30] K.-H. Ahn, A. Hariki, K.-W. Lee, and J. Kuneš, Physical Review B **99**, 184432 (2019), arXiv:1902.04436.

[31] L. Néel, Reviews of Modern Physics **25**, 58 (1953).

[32] A. T. Costa, R. B. Muniz, and D. L. Mills, Physical Review B **68**, 224435 (2003).

[33] K. Yosida, *Theory of Magnetism* (Springer Berlin, Heidelberg, 1996).

[34] Y. Kakehashi, *Modern Theory of Magnetism in Metals and Alloys*, Springer Series in Solid-State Sciences, Vol. 175 (Springer Berlin Heidelberg, Berlin, Heidelberg, 2013).

[35] H. Ebert, D. Ködderitzsch, and J. Minár, Reports on Progress in Physics **74**, 096501 (2011).

[36] J. Haines, J. M. Léger, O. Schulte, and S. Hull, Acta Crystallographica Section B Structural Science **53**, 880 (1997).

[37] T. Berlijn, P. C. Snijders, O. Delaire, H.-D. Zhou, T. A. Maier, H.-B. Cao, S.-X. Chi, M. Matsuda, Y. Wang, M. R. Koehler, P. R. C. Kent, and H. H. Weitering, Physical Review Letters **118**, 077201 (2017), arXiv:1612.09589.

[38] X. He, N. Helbig, M. J. Verstraete, and E. Bousquet, Computer Physics Communications **264**, 107938 (2021), arXiv:2009.01910.

[39] Q. Cui, B. Zeng, T. Yu, H. Yang, and P. Cui, , 1 (2023), arXiv:2306.08976.